https://doi.org/10.5194/acp-2021-941
Preprint. Discussion started: 5 January 2022

Atmospheric Chemistry and Physics Discussions

Aerosol Atmospheric Rivers:

Climatology, Event Characteristics, and Detection Algorithm Sensitivities

Sudip Chakraborty[1*], Bin Guan[1,2], Duane E. Waliser[1], Arlindo M. da Silva[3]

[1]Jet Propulsion Laboratory, California Institute of Technology, Pasadena, CA, USA

[2]Joint Institute for Regional Earth System Science and Engineering, University of California, Los Angeles, CA, USA

[3] Global Modeling and Assimilation Office, NASA/Goddard Space Flight Center, Greenbelt, MD, USA

*Corresponding Author email: sudip.chakraborty@jpl.nasa.gov

https://doi.org/10.5194/acp-2021-941
Preprint. Discussion started: 5 January 2022

Atmospheric Chemistry and Physics Discussions

Abstract

Leveraging the concept of atmospheric rivers (ARs), a detection technique based on a widely utilized global algorithm to detect ARs (Guan et al., 2018; Guan and Waliser, 2015, 2019) was recently developed to detect aerosol atmospheric rivers (AARs) using the Modern-Era Retrospective analysis for Research and Applications, Version 2 reanalysis (Chakraborty et al., 2021a). The current study further characterizes and quantifies various details of AARs that were not provided in that study, such as AARs' seasonality, event characteristics, vertical profiles of aerosol mass mixing ratio and wind speed, and the fraction of total annual aerosol transport conducted by AARs. Analysis is also performed to quantify the sensitivity of AAR detection to the criteria and thresholds used by the algorithm. AARs occur more frequently over, and typically extend from, regions with higher aerosol emission. For a number of planetary-scale pathways that exhibit large climatological aerosol transport, AARs contribute 40-80% to the total annual transport. DU AARs are more frequent in boreal spring, SS AARs are often more frequent during the boreal winter (summer) in the Northern (Southern) Hemisphere, CA AARs are more frequent during dry seasons and often originate from the global rainforests and industrial areas, and SU AARs are present in the Northern Hemisphere during all seasons. For most aerosol types, the mass mixing ratio within AARs is highest near the surface and decreases monotonically with altitude. However, DU and CA AARs over or near the African continent exhibit peaks in their aerosol mixing ratio profiles around 700 hPa. AAR event characteristics are mostly independent of species with mean length, width, and length/width ratio around 4000 km, 600 km, and 8, respectively.

https://doi.org/10.5194/acp-2021-941
Preprint. Discussion started: 5 January 2022

Atmospheric Chemistry and Physics Discussions

1. Introduction

As an important component of atmospheric composition, aerosols have considerable impacts on the convective lifetime and precipitation (Andreae and Rosenfeld, 2008; Chakraborty et al., 2016; Fan et al., 2016; Rosenfeld et al., 2008, 2013, 2014, 2016; Seinfeld et al., 2016; Stevens and Feingold, 2009), the radiation budget via direct and indirect effects (Chylek and Wong, 1995; Huang et al., 2006; Kim and Ramanathan, 2008; Lohmann and Feichter, 2001; Takemura et al., 2005), and the hydrological cycle (e.g. Chakraborty et al., 2018; Rosenfeld et al., 2008). In particular, their interactions with cloud microphysics and radiative forcing remain highly uncertain, constituting a large uncertainty in the assessment of climate radiative forcing (IPCC, 2013b, 2013a). Furthermore, aerosols have been identified to impact photosynthesis either by modulating the direct beam photosynthetically active radiation (Xi and Sokolik, 2012) or by decreasing the direct sunlight due to attenuation (Wang et al., 2021). Moreover, aerosols degrade the air quality and visibility, thus pose direct and negative impacts on human health (Gupta and Christopher, 2009; Li et al., 2017; Martin, 2008; Wang and Christopher, 2003).

With the advent of satellites capable of providing global-scale observations, it has become clear that aerosol loading in the atmosphere is not limited to regions just near their emission sources, but are also transported across continental areas and large expanses of the ocean — emphasizing a source-receptor relationship among these impacts of aerosols. Leveraging the concept of atmospheric rivers (ARs) (Ralph et al., 2020; Zhu and Newell, 1994) and a widely used global AR detection algorithm (Guan et al., 2018; Guan and Waliser, 2015, 2019), our previous study developed an aerosol atmospheric rivers (AARs) detection algorithm (Chakraborty et al., 2021a). That study applied the new AAR detection algorithm to five primary aerosol species represented in the MERRA-2 reanalysis – dust (DU), sulfate (SU), sea salt (SS),

https://doi.org/10.5194/acp-2021-941
Preprint. Discussion started: 5 January 2022


Atmospheric Chemistry and Physics Discussions

and organic and black carbon (CA), and showed that aerosols can be transported long distances by AARs, i.e. narrow and elongated channels of very high values of vertically-integrated aerosol transport. Moreover, it was found that depending on the region and aerosol species, AARs can be responsible for 40-80% of the total annual aerosol transport in only 20-30 AAR days per year, on average. That study also illustrated that AAR events can have profound impacts on local air quality conditions.

Owing to the relatively large contribution AARs have on the total annual aerosol transport in many regions across the world, and the impacts that AARs can have on regional air quality conditions, it is important to further investigate and quantify the roles AARs play within the climate system and the impacts they have on air quality. For example, our previous study did not characterize and show the vertical profiles of aerosol mass flux and wind of AARs for each aerosol species. However, such information is crucial to improving the understanding of the impacts of aerosols on the global radiative budget since multiple studies have revealed that the aerosols' radiative impact depends on the aerosol composition and their vertical distribution (Keil and Haywood, 2003; McComiskey and Feingold, 2008; Mishra et al., 2015; Satheesh and Ramanathan, 2000). With that motivation in mind, the current study explores the AAR concept further, characterizing and quantifying additional important features of AARs that were not provided in Chakraborty et al. (2021a). These include 1) characteristics of individual AARs such as length, width, length/width ratio, transport strength, and dominant transport direction, 2) seasonal variations, 3) relationship to the spatial distribution of surface emissions, 4) vertical profiles of wind, aerosol mixing ratio, and aerosol mass fluxes, and 5) the major planetary-scale aerosol transport pathways AARs contribute to. As with Chakraborty et al (2021a), we carry out this analysis utilizing the Modern-Era Retrospective analysis for Research and Applications,

https://doi.org/10.5194/acp-2021-941
Preprint. Discussion started: 5 January 2022


Atmospheric Chemistry and Physics Discussions

Version 2 (MERRA-2) reanalysis during 1997-2014, and for all five aerosol species represented: dust (DU), sulfate (SU), sea salt (SS), and organic and black carbon; the latter two are combined into carbonaceous aerosols (CA) in Figures 1 and 2 (Buchard et al., 2017; Gelaro et al., 2017; Randles et al., 2017).

2. Data

For this study, we use the MERRA-2 aerosol reanalysis (Global Modeling and Assimilation Office (GMAO), 2015a; last accessed : June 2021) that has a horizontal resolution of 0.5° x 0.625° and a temporal resolution of 1 hour (Randles et al., 2017). In particular, most of the analysis is based on the zonal and meridional components of the vertically-integrated aerosol mass flux data. For example, we have used the variables DUFLUXU and DUFLUXV to compute integrated aerosol transport (IAT) values for dust at each grid. The MERRA-2 aerosol reanalysis data capture the global aerosol optical depth reasonably well and are well-validated by many studies using observation (Aldabash et al., 2020; Carra et al., 2020; Gueymard and Yang, 2020). MERRA-2 aerosol data have previously been used in studies investigating aerosol microphysical effect and global aerosol transport (Chakraborty et al., 2021a; Sitnov et al., 2020; Xu et al., 2020). Our previous study using MERRA-2 data successfully detected AARs over various regions of the globe, and the AERONET stations located either in the receptor regions or along the path of AARs have shown a substantial increase in the aerosol optical thickness during AAR events (Chakraborty et al., 2021a).

To examine the vertical profiles of aerosol amount, wind and aerosol mass fluxes (i.e. Figure 4), we use MERRA-2 3-hourly, instantaneous, aerosol mixing ratio data (inst3_3d_aer_Nv, last accessed : June 2021) that provide aerosol mass mixing ratio at 72 vertical levels. To assess the information about the zonal and meridional wind, we use MERRA-2's associated meteorological

https://doi.org/10.5194/acp-2021-941
Preprint. Discussion started: 5 January 2022

Atmospheric Chemistry and Physics Discussions

fields (inst3_3d_asm_Nv, last accessed : June 2021) with the same resolution as the aerosol mass mixing ratio data (Randles et al., 2017). In addition, we also use MERRA-2 time-averaged, single-level, assimilated aerosol diagnostics (Global Modeling and Assimilation Office (GMAO), 2015b, last accessed : June 2021) datasets to describe the spatial distribution of the emissions of aerosol particles at the surface to examine the relationship between source regions and frequency of occurrence of AARs.

3. Methodology

The AR detection algorithm designed by Guan and Waliser (2015) was to detect and study ARs based on a combination of criteria related to the intensity, direction, and geometry of vertically integrated water vapor transport (IVT). The algorithm and associated AR detection databases (based on multiple reanalysis products) have been widely used by the AR research community (e.g., Chapman et al., 2019; Dhana Laskhmi & Satyanarayana, 2020; Edwards et al., 2020; Gibson et al., 2020; Guan et al., 2020a; Guan & Waliser, 2019; Huning et al., 2019; Jennrich et al., 2020; Nash & Carvalho, 2019; Sharma & Déry, 2020; Wang et al., 2020; Zhou & Kim, 2019; https://ucla.app.box.com/v/arcatalog/file/700858122185). Details about the AAR algorithm and the modifications made to the AR algorithm to make it applicable for AARs are provided below.

In the initial AAR algorithm (Chakraborty et al., 2021a), we detect AARs daily at four-time steps (00, 06, 12, and 18 hours UTC) for a period of 18 years during 1997-2014 and separately for each aerosol species. To compute total IAT over each grid cell at each time step for any species (n) of aerosols we calculate $IAT_n = \sqrt[2]{IATU_n^2 + IATV_n^2}$ where IATU and IATV denote the vertically integrated aerosol mass flux in the zonal and meridional directions, respectively. We are interested in identifying extreme transport events; thus, we first compute the 85th

https://doi.org/10.5194/acp-2021-941
Preprint. Discussion started: 5 January 2022


Atmospheric Chemistry and Physics Discussions

139 percentile of the IAT magnitude over each grid cell during 1997-2014. Grid cells with IAT
140 magnitude less than the 85th percentile threshold are discarded. The remaining grid cells serve as
141 input to the following five steps to 1) isolate objects (i.e., contiguous areas) of enhanced IAT
142 with values above the 85th percentile; 2) check the consistency of the IAT directions at each grid
143 cell within an IAT object, to retain only those objects where at least 50% of the grid cells have
144 IAT directions within 45° of the direction of the mean IAT of the entire object; 3) retain the
145 stronger 50% of those objects detected in the previous step based on the object-mean IAT; 4)
146 retain objectives only if the direction of object-mean IAT is within 45° of the along-river axis to
147 ensure that the direction of the aerosol transport is aligned with the river; 5) apply length and
148 length-to-width ratio criteria and retain only those objects longer than 2000 km an aspect ratio
149 greater than 2. At the end of these steps, the objects that remain are referred to as AARs and are
150 further characterized in this study. We also show the sensitivity of the detection of AARs to key
151 threshold values used in the above steps in Figure 9.

152 In developing the AAR detection algorithm (Chakraborty et al., 2021a), only three changes
153 were made to the original AR detection algorithm. In step 1 of the AR moisture algorithm, a
154 fixed lower limit of IVT, specifically 100 kg m^{-1} s^{-1}, is applied globally to facilitate detection of
155 ARs in polar regions where IVT is extremely weak climatologically due to the very cold, dry
156 atmosphere. We found that this additional filter is not needed for AAR detection. In addition,
157 given the strong meridional moisture gradient between the tropics and extratropics, ARs are
158 primarily recognized as the dominant means to transport water vapor poleward (Zhu and Newell,
159 1998). Accordingly, the AR algorithm is designed to detect IVT objects with notable transport in
160 the poleward direction. However, since there is no similar and dominant planetary gradient in
161 aerosol concentration in the north-south direction, we removed this constraint on meridional IAT

https://doi.org/10.5194/acp-2021-941
Preprint. Discussion started: 5 January 2022


Atmospheric Chemistry and Physics Discussions

for AARs and instead applied a constraint on the total IAT (i.e., zonal and meridional components combined). Finally, Chakraborty et al. (2021a) computed the climatological 85th percentile threshold IAT values for each month based on the 5 months centered on that month, as in the original AR algorithm (Guan and Waliser, 2015). However, it was found that a 3-month window better resolves the annual cycle of IAT and meanwhile still retains sufficient sampling over the period of 1997–2014. For example, the IAT 85th percentile for February is calculated using the IAT values four times each day during January-March of 1997-2014.

AAR frequency at each grid cell is calculated as percent of time steps AARs are detected at that grid cell, and expressed in units of days/year for annual means (by multiplying the percentage by 365 days/year) and days/season for seasonal means (by multiplying the percentage by 91 days/season). The mean zonal and meridional IAT associated with AARs over each grid cell at latitude φ and longitude λ are calculated as:

$Mean\ IATU(\varphi,\lambda) = \sum_1^N IATU\ (\varphi,\lambda)$/N and $Mean\ IATV(\varphi,\lambda) = \sum_1^N IATV\ (\varphi,\lambda)$/N

where N is the number of times AARs were detected over that grid cell.

To obtain the fraction of total (i.e., regardless of AAR or non-AAR) annual transport conducted by AARs of five different aerosol species, we first temporally integrate IATU and IATV over all the time steps when AARs were detected over a grid cell at latitude φ and longitude λ as

$$Total\ IATU(\varphi,\lambda) = \int_0^T IATU(\varphi,\lambda,t)\,dt \quad (1a)$$

$$Total\ IATV(\varphi,\lambda) = \int_0^T IATV(\varphi,\lambda,t)\,dt \quad (1b)$$

where dt is the duration between each time step (6 hours), and T is the total duration for 18 years. Based on that, the magnitude of annual AAR IAT, which is a scalar quantity, at each grid cell is calculated as $Total\_AAR\_annual\_IAT_{\varphi,\lambda} = \sqrt[2]{Total\ IATU(\varphi,\lambda)^2 + Total\ IATV(\varphi,\lambda)^2}/18$.

https://doi.org/10.5194/acp-2021-941
Preprint. Discussion started: 5 January 2022


Atmospheric Chemistry and Physics Discussions

Similarly, we compute $Total\_all\_annual\_IAT_{\varphi,\lambda}$ for all the time steps (i.e., AAR and non-AAR combined). Next, since the annual AAR IAT and annual total IAT are not expected to be in the same exact direction, we project the former onto the latter. For that, the directions of the two vectors are obtained as

$$ß_{All} = \tan^{-1}(Total\ IATU(\varphi,\lambda)/Total\ IATV(\varphi,\lambda)) \text{ for all events} \quad (2a).$$

$$ß_{AAR} = \tan^{-1}(Total\ IATU(\varphi,\lambda)/Total\ IATV(\varphi,\lambda)) \text{ for AAR events} \quad (2b).$$

Finally, the fraction of total annual transport conducted by AARs is obtained as $Frac_{\varphi} = Total\_AAR\_annual\_IAT_{\varphi,\lambda} \times \cos(ß)/Total\_all\_annual\_IAT_{\varphi,\lambda}$, where $ß = ß_{All} - ß_{AAR}$.

4. Results

4.1 Overall aerosol transport and surface emission

To provide a background for characterizing the seasonality of AARs, we first illustrate the seasonal variability of the overall aerosol transport (i.e., regardless of AAR conditions) during 1997-2014 (Fig. 1). Here, we combine black carbon (BC) and organic carbon (OC) aerosols, denoted as CA, owing to their similar sources and seasonality (BC and OC are accounted for separately in subsequent analysis of AARs). Dust IAT (first column, Fig. 1) is higher during the MAM and JJA seasons. Global deserts, such as the Sahara Desert, Gobi Desert, and Taklamakan Desert and the Middle East act as a significant source of dust aerosols year-round (Fig. 2A) emitting more than 2 x 10^{-9} kg m^{-2} s^{-1} of dust, primarily in the northern Spring. The sea-salt IAT (second column, Fig.1) increases during the winter seasons of the Northern and Southern Hemispheres due to the increased mean westerly flow and storm activities during these seasons. Annual maps of SS emission (Fig. 2B) show that a large number of SS aerosols are emitted over

https://doi.org/10.5194/acp-2021-941
Preprint. Discussion started: 5 January 2022

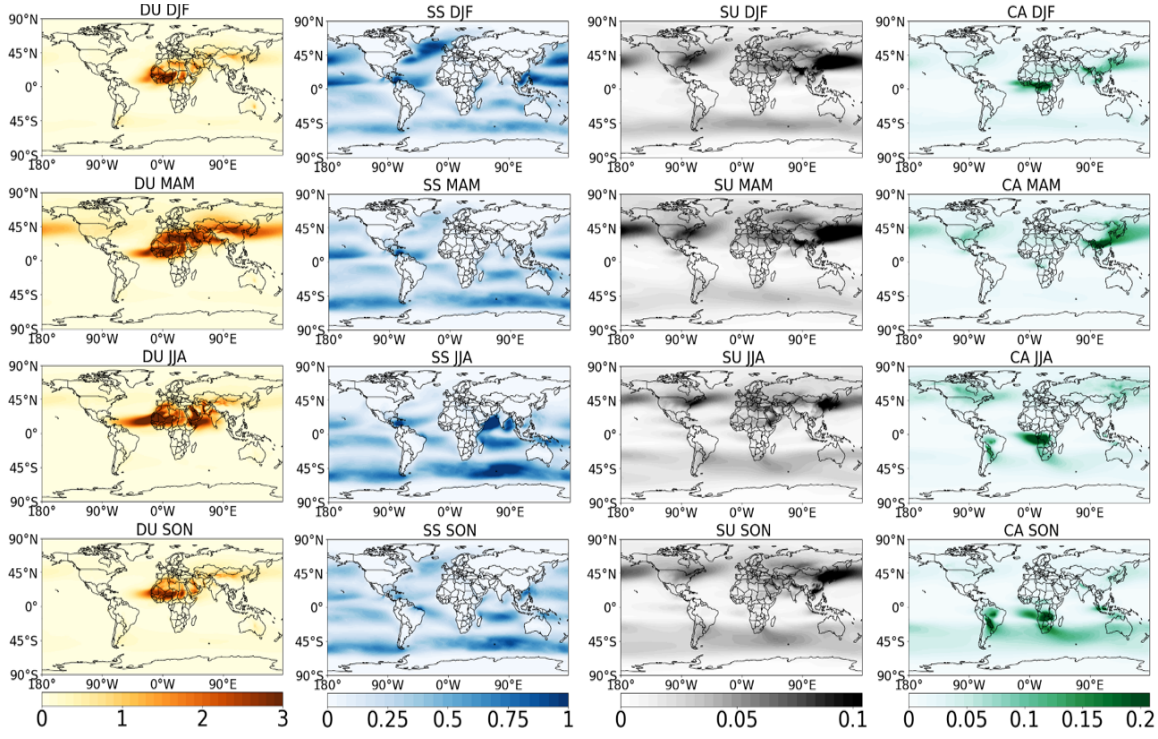

Figure 1. MERRA-2 vertically integrated aerosol transport (IAT, 10^{-3} kg m^{-1} s^{-1}) in 4 seasons (DJF: December-February; MAM: March-May; JJA: June-August, and SON: September-November) during 1997-2014.

the global oceans, especially over the tropical oceans because of the convective activities and in the midlatitudes where synoptic storm activities are dominant. Sulfate IAT (SU, third column, Fig. 1) is high over a region between China and the North Pacific Ocean region, extending up to the western US, during all seasons with the lowest SU IAT values in JJA. The large SU IAT values (Figure 2C) are likely due to high emissions of SU over China (Dai et al., 2019; Wang et al., 2013) coupled with strongly varying synoptic flows. A secondary region of higher amount of SU IAT is also detected between the eastern US and the northwestern Atlantic Ocean as many SU aerosols are emitted east of the Rocky Mountains, particularly over the Ohio valley (Fig. 2C). Figure 2C also shows some SU aerosols emitted due to global shipping activities.

https://doi.org/10.5194/acp-2021-941
Preprint. Discussion started: 5 January 2022

Atmospheric Chemistry and Physics Discussions

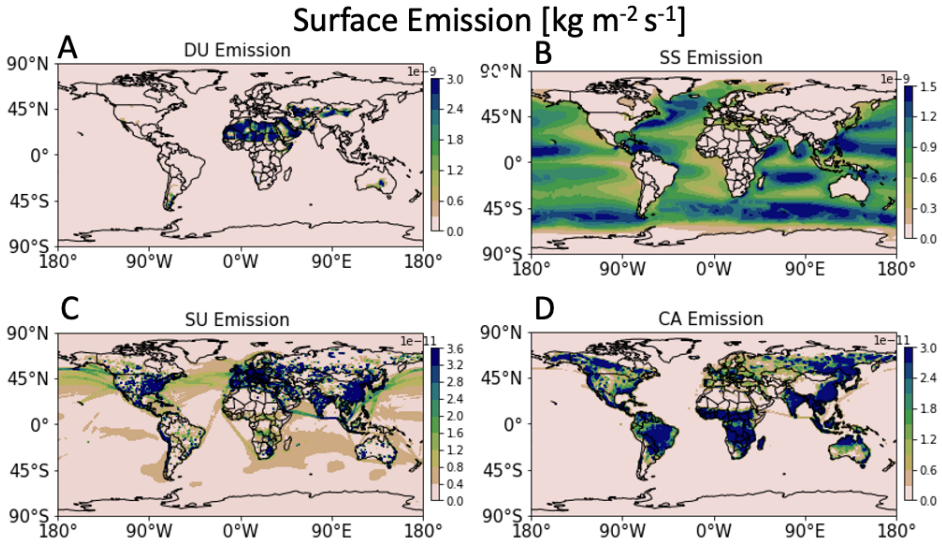

Figure 2. Annual surface emission (kg m^{-2} s^{-1}) of (A) DU, (B) SS, (C) SU and (D) CA (BC+OC) aerosol species during 1997-2014 from the MERRA-2 data.

Global rainforests are the most significant contributors to the CA aerosols (Fig. 2D). Accordingly, it appears that the Congo rainforest dominates the Amazon rainforest in terms of CA IAT (right column, Fig. 1). The Amazon rainforest region has higher IAT during its dry and transition seasons, and lower IAT in the wet season. Similarly, the Congo rainforest releases a high amount of CA aerosols during the dry season (JJA) and another peak in the Sahel during DJF (Fig. 2D). An increase in dry period CA IAT might be due to the increased vegetative stress, forest fire, and agricultural burning over these two regions. However, it is interesting to note that the Congo rainforest also emits CA aerosols during the boreal autumn (SON) rainy season, which is the stronger of the two rainfall seasons in this region, but not during the MAM rainy season. In MAM, the tropical rainforests over eastern India, Myanmar, and southern China have higher CA IAT values. A significant amount of CA aerosols are also emitted in the midlatitudes in the Northern Hemisphere (Fig. 2D), but the IAT values over there are low in all four seasons

https://doi.org/10.5194/acp-2021-941
Preprint. Discussion started: 5 January 2022


Atmospheric Chemistry and Physics Discussions

(Fig. 1). These results point out the existence of seasonality and variability in the overall aerosol emission and transport. As a result, we expect the frequency and intensity of AARs might also vary among different seasons in accordance with the distribution of surface emissions.

4.2 AAR frequency and intensity

To illustrate characteristics of individual AAR objects, Fig. 3 shows examples of AARs of each species, including the location, shape, and transport direction and magnitude. Also indicated in the figure is the length and width of each illustrated AAR. Figure 3A shows all the DU AARs detected on 25th June, 2008 at 1200 UTC. Many of those DU AARs are detected between the Sahara Desert and the Caribbean, the middle east region and Europe, over the central US, and over the Patagonia region. Figure 3D shows details of one DU AAR (encircled in Fig. 3A) that extends from the western boundary of the Sahara Desert to the southern US and Caribbean and has IAT values greater than 12 x 10^{-3} kg m^{-1} s^{-1}. The AAR is 8082 km long and 1158 km wide. Similarly, we show details of one SS AAR (Fig. 3E) with a length of 5295 km and a width of 984 km (IAT ~ 1.0 x 10^{-3} kg m^{-1} s^{-1}) over the Southern Ocean among other AARs detected on 19th January 2010 at 1200 UTC (Fig. 2B). Unlike DU AARs, SS AARs are located mostly over the ocean (see also Fig. 4) and carry the extratropical AR signature. SS AARs over the tropical regions appear to be smaller than the extratropical AARs in Figure 3B.

A number of SU AARs occurred in the polar region due to the Eyjafjallajökull volcanic eruption (Fig. 3C). The volcano, located in Iceland, erupted on the 20th March 2010, causing disruption to the aviation industry (https://volcanoes.usgs.gov/volcanic_ash/ash_clouds_air_routes_eyjafjallajokull.html). In Figure 3F, we show details of one of these SU AARs on the 29th March 2010. The SU AAR is 6203 km

https://doi.org/10.5194/acp-2021-941
Preprint. Discussion started: 5 January 2022

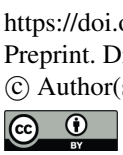

Atmospheric Chemistry and Physics Discussions

long and 294 km wide and transported a large amount of SU aerosols (IAT ~ 0.1 x 10^{-3} kg m^{-1} s^{-1}) into and across the polar region. It is important to notice that MERRA-2 did not include the ash aerosols that were co-emitted with the SO_2 plumes that were eventually converted into sulfate aerosols by gaseous and aqueous processes. Figure 3G shows examples of OC AARs detected on

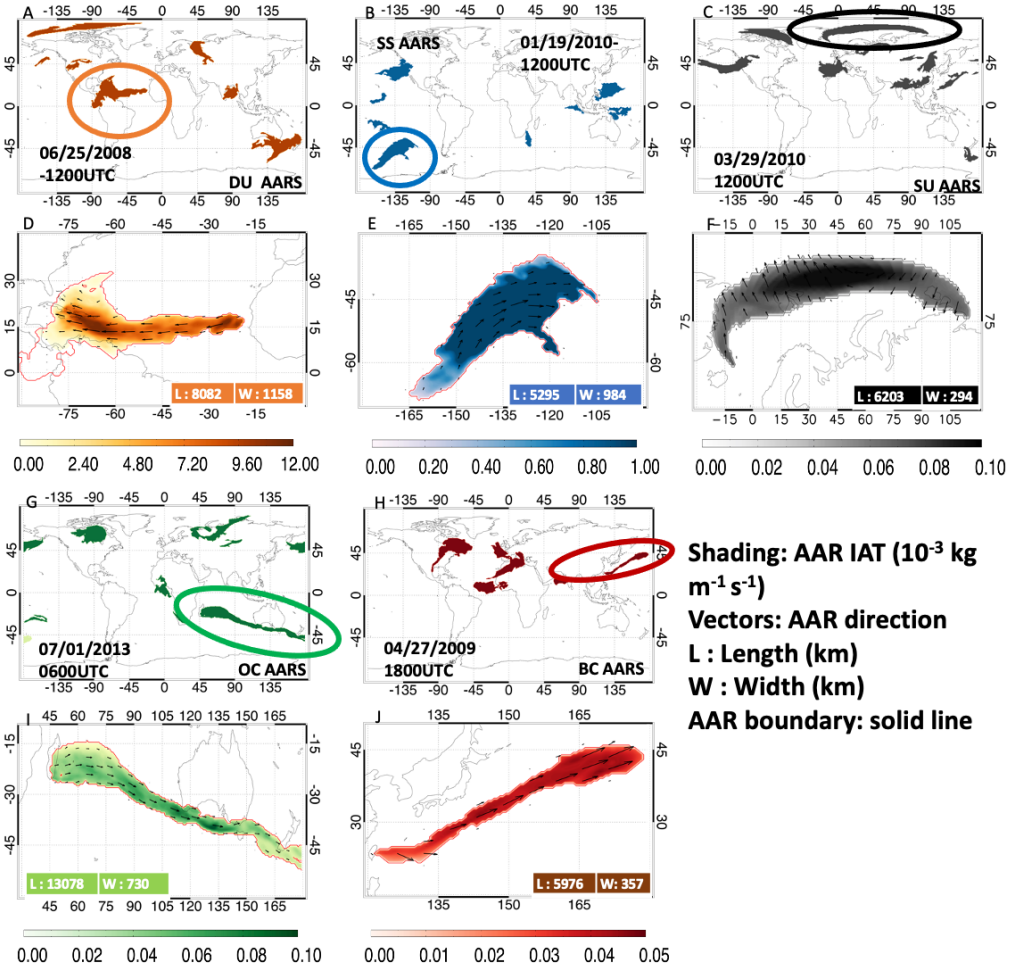

Figure 3: Detection of five different species of aerosols atmospheric rivers. Each panel in the 1st and 3rd rows show all AARs detected for a given species at an arbitrary time step; see bottom of each panel for the aerosol species and time stamp. Each panel in the 2nd and 4th rows shows detail (see legend) of a specific AAR from the corresponding panel above.

https://doi.org/10.5194/acp-2021-941
Preprint. Discussion started: 5 January 2022


Atmospheric Chemistry and Physics Discussions

255 the 1st July 2013. We show details of one OC AAR that stretches from Madagascar to New
256 Zealand in Figure 3I. The OC AAR is 13078 km long and 730 km wide and flows west over the
257 Indian Ocean with IAT of ~0.1 x 10^{-3} kg m^{-1} s^{-1}. Figure 3H shows a few BC AARs detected on
258 27th April 2009. BC AARs often originate near the China-northwestern Pacific Ocean region (see
259 also Fig. 4). We show the details of one such BC AAR in Figure 3J. It is to be noted that the IAT
260 values of BC AARs are smaller than the OC AARs in terms of AOD; however, they might play a
261 significant role in the atmospheric radiation budget owing to the capability of BC aerosols to
262 absorb solar energy.

263 To illustrate the overall climatology of AARs, Figure 4 shows the annual mean frequency of
264 occurrence (shading; days per year) and the mean IAT (arrows; kg m^{-1} s^{-1}) associated with AARs.
265 Figure 4A shows that a strong anticyclonic motion over the Sahara Desert is associated with
266 many DU AARs, consistent with the annual DU emission (Fig. 2A) and seasonal DU IAT (Fig. 1
267 – leftmost column) over that region. Around 30 AAR days/year (shades) carry on average 3-15 x
268 10^{-3} k gm^{-1} s^{-1} (vectors) of dust from the Sahara Desert over the North Atlantic Ocean and reach
269 the southern US and the Caribbean regions. A similar number of AARs also transport aerosols
270 towards Europe and the middle east region. A relatively high number of DU AARs are detected
271 over China, Mongolia, and Kazakhstan; however, the mean transport over these regions by
272 AARs is lower (IAT ~1 x 10^{-3} kg m^{-1} s^{-1}) than those originating from the Sahara Desert. The
273 Southern Hemispheric deserts also emit numerous AARs but with a smaller amount of dust
274 transport as the dust emission (Fig. 2A) and IAT (Fig. 1) are low over there. Overall, the Sahara
275 Desert dominates any other deserts in the world regarding the formation of the strongest and
276 most intense DU AARs.

https://doi.org/10.5194/acp-2021-941
Preprint. Discussion started: 5 January 2022

Atmospheric Chemistry and Physics Discussions

277 Figure 4B shows the climatological maps of SS AARs. SS AARs are mostly located over the
278 global oceans, especially over the tropical and subtropical trade wind regions. The SS AARs in
279 the midlatitudes carry the signature of the storm tracks, and have distributions similar to ARs
280 (Guan and Waliser, 2015). Around 20 AAR days/year occur in the mid-latitudes with mean IAT
281 of ~2 x 10^{-3} kg m^{-1} s^{-1}. In comparison, tropical SS AARs are more frequent but have less IAT than
282 the midlatitude SS AARs. Around 30 SS AARs have mean IAT of ~1 x 10^{-3} kg m^{-1} s^{-1} over the
283 tropical region.

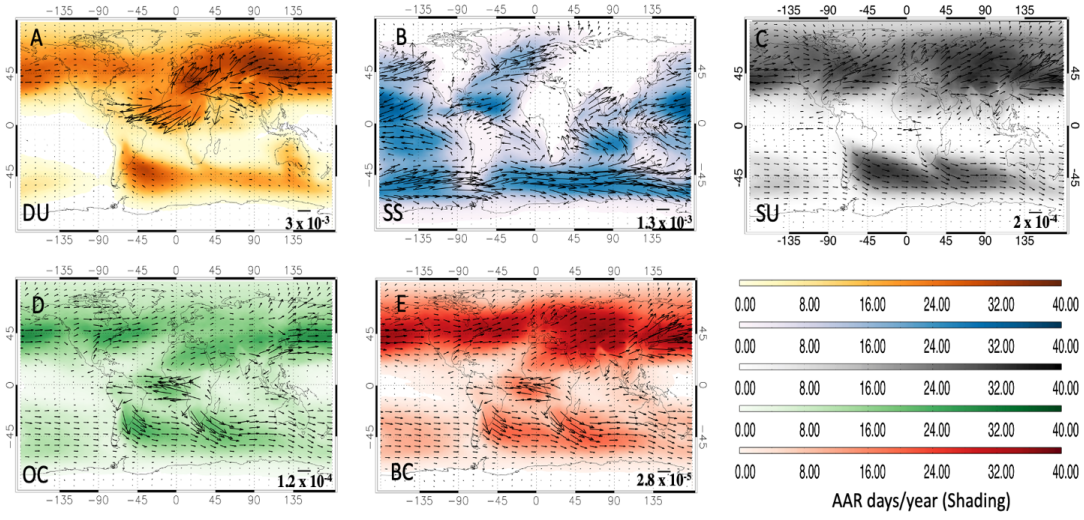

Figure 4. Annual climatological AAR frequency (days/year; shading) and IAT (arrows; kg m^{-1} s^{-1}) during 1997-2014 based on MERRA-2. (A) Dust; (B) Sea salt; (C) Sulfate; (D) Organic carbon; (E) Black carbon. Scales for the IAT vectors are provided in the lower right side of each plot.

284 It is important to note SU AARs are more frequent (~40 days/year, Fig. 4C) in the Northern
285 Hemisphere than in the Southern Hemisphere, consistent with the predominance of emissions of
286 SU aerosols over China, Europe, and the eastern US (Fig. 2C) owing to anthropogenic emissions
287 as well as biogenic activities in these regions. It is important to note that MERRA-2 aerosols data
288 don't account for biogenic sources like Carbonyl Sulfide and Dimethyl Sulfate. The primary

https://doi.org/10.5194/acp-2021-941
Preprint. Discussion started: 5 January 2022


Atmospheric Chemistry and Physics Discussions

289 regions of higher SU AAR activity include the eastern US, Europe, and eastern China. The SU
290 AAR hotspot regions over the Southern Hemisphere include pathways from the southern edges
291 of the global rainforests to the South Indian, South Atlantic, and Southern Oceans. Mean IAT
292 (~0.2 x 10^{-3} kg m^{-1} s^{-1}) by SU AARs is lower than that of the DU and SS AARs. Many BC and
293 OC AARs originate from the global rainforests, such as the Congo and Amazon, and from the
294 regions that are susceptible to biomass burning and CA aerosol emissions, such as Europe, the
295 eastern US, industrialized areas over eastern China, and north India. Annually, 20-40 BC or OC
296 AARs are generated from these regions. It appears that BC AARs are more numerous than the
297 OC AARs; however, OC AARs have larger IAT than BC AARs.

298 **4.3 Vertical profiles of AAR aerosol mass flux and wind**

299 To understand the anomalous atmospheric conditions that account for an AAR event, it is
300 important to know the relative contribution of the two quantities that make up these IAT
301 extremes, namely the aerosol mixing ratio and the wind speed. Also, as mentioned before, the
302 altitude of aerosol particles within AARs can be of importance due to aerosol impacts on the
303 radiation budget, convective anvil lifetime (Bister and Kulmala, 2011), cloud formation (Froyd
304 et al., 2009; Khain et al., 2008), and air quality near the surface. Here, we characterize the
305 vertical profiles of the AARs at a number of different locations with high AAR frequency (see
306 the inset map in the middle column; based on Fig. 4). It is important to keep in mind that the
307 aerosol vertical structure in MERRA-2 are not directly constrained by measurements, and are
308 chiefly determined by the injection height of the emissions as well as turbulent and convective
309 transport processes parameterized in the model; evaluation of the vertical structure of MERRA-2
310 aerosols appear in Buchard et al. (2017). The left column of Fig. 5 shows composite vertical

https://doi.org/10.5194/acp-2021-941
Preprint. Discussion started: 5 January 2022

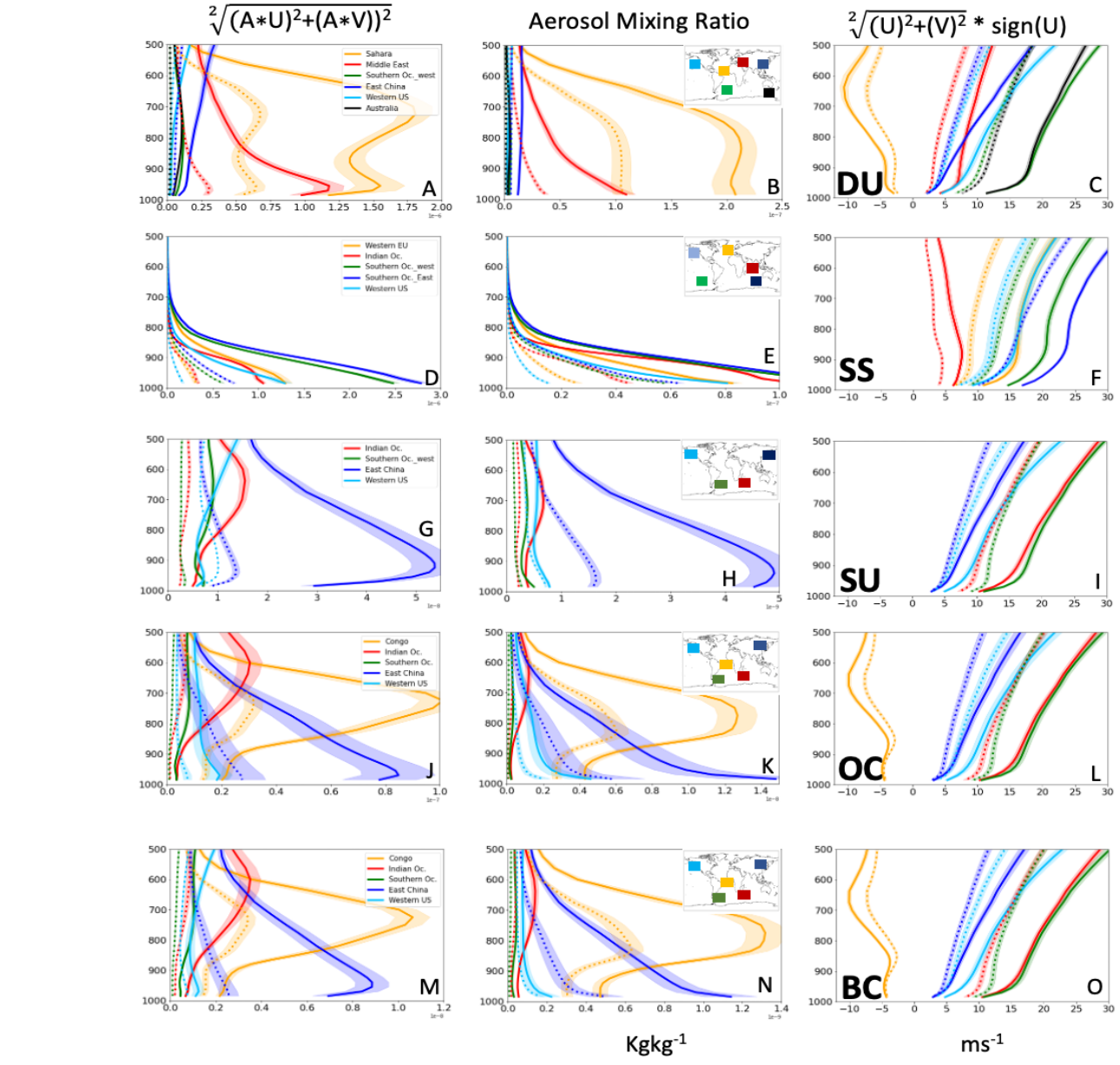

Figure 5. Average vertical profiles of (left) aerosol mass fluxes, (center) aerosols mixing ratio, and (right) wind speed over a number of locations for AAR events (solid) and All (dotted) time steps. Please see the AAR frequency maps in the inset of the middle panel for the locations chosen to calculate the profiles. In the right column, a sign convention (see column title) is used to highlight the general east-west direction of the wind speed profiles.

311 profiles of aerosol mass fluxes for each aerosol species; both those for AARs (solid) and for all

https://doi.org/10.5194/acp-2021-941
Preprint. Discussion started: 5 January 2022


Atmospheric Chemistry and Physics Discussions

312 time steps regardless of AAR conditions (dotted) are shown for comparison. Mean fluxes of the
313 synoptic AAR events is larger than the overall annual mean over all the regions, not unexpected
314 since AARs represent the extreme transport events. For DU AARs (Fig. 5A), the strongest
315 transport is observed between the Sahara Desert and North Atlantic/Caribbean (orange) as well
316 as western Europe/middle-east (red) pathways. Flux values decreases with altitude within AARs
317 that transport aerosols from the Sahara Desert to the Europe/Middle East region(red). However,
318 AARs that transport aerosols from the Sahara Desert to the North Atlantic region (orange) have
319 peak IAT values near 750 hPa.

320 We also show the vertical aerosol mixing ratio profiles (middle column) and the wind
321 profiles (right column) separately to help disentangle their influences on the aerosol flux profiles.
322 Figure 5B shows that high aerosol levels inside AARs over the Sahara Desert-Caribbean
323 pathway extend vertically up to the 700 hPa with a peak around 750 hPa, unlike any other
324 regions analyzed. The third column, which shows the mean wind speed profile $\sqrt[2]{U^2+V^2}$
325 multiplied by the sign of the zonal wind to show the east-west direction of the AARs, confirms
326 the influence from the African easterly jet-north or AEJ-N (Cook, 1999; Wu et al., 2009) on
327 AARs' wind profile that peaks around 650 hPa and lifts aerosols over this region (Fig. 4C).
328 Higher flux values near the surface are due to a high aerosol mixing ratio, but as altitude
329 increases higher flux values inside AARs is contributed by both the aerosol lifting and the high
330 zonal wind speed of AEJ-N between the Sahara Desert and the North Atlantic Ocean region.
331 Other regions like the Southern Ocean (near South America), Australia, eastern China, and
332 western US have less aerosol mixing ratio as compared to the Sahara-the North Atlantic
333 Ocean/Caribbean and Sahara-Europe/Middle east pathways. Wind speed contributes to larger
334 flux values as altitude increases over some of these locations near eastern China, the Southern

https://doi.org/10.5194/acp-2021-941
Preprint. Discussion started: 5 January 2022


Atmospheric Chemistry and Physics Discussions

335 Ocean, Australia, and the western US, however, their flux values are less than those taking off
336 the Sahara Desert.

337 Aerosol flux and mass mixing ratio profiles for SS species (Figs. 5D and 5E) decreases with
338 altitude. This is because the SS particles are typically found within the boundary layer (Gross
339 and Baklanov, 2007) and are larger in size, and often form due to high wind speed and surface
340 evaporation along the storm tracks and may not travel long distances outside the storm tracks
341 (May et al., 2016; Sofiev et al., 2011). The largest aerosol mixing ratio and IAT values are
342 observed over the Southern Ocean consistent with the persistent and year-round AAR activities
343 over there.

344 Consistent with the SU aerosol emission (Fig. 2C), eastern China (blue line) dominates in
345 terms of SU aerosol mass mixing ratio by a factor of 5 as compared to the other regions (Fig. 5H)
346 analyzed and shown here. The aerosol mixing ratio (Fig. 5H) and the flux values (Fig. 5G)
347 increase with height, attain a peak around 900 hPa over there, probably exhibiting a boundary
348 layer inversion effect due to industrial pollutants (Li et al., 2017). Above 900 hPa, both the
349 aerosols mass mixing ratio and flux values gradually decrease. Flux profiles and aerosols mixing
350 ratio over the Indian Ocean (red) and Southern Ocean (green) show different behavior. Aerosols
351 appear to be continental in origin and are lifted to attain a peak concentration around 650 hPa.
352 Contribution from wind speed (Fig. 5I) as compared to aerosol mixing ratio (Fig. 5H) appears to
353 be less on the SU flux profiles (Fig. 5G) since the wind speed associated with AARs is the
354 highest over the Indian and Southern Ocean, but the largest flux values are associated with the
355 AARs over the eastern China region which have the largest aerosol mass mixing ratio.

356 Next, we examine the vertical profiles of CA AARs over the Congo basin, the western US,
357 the eastern China, the Indian Ocean, and the Southern Ocean. As in the case of dust aerosols over

https://doi.org/10.5194/acp-2021-941
Preprint. Discussion started: 5 January 2022


Atmospheric Chemistry and Physics Discussions

the Sahara Desert – North Atlantic transport pathway (Fig. 5A, orange line), both the OC and BC AARs off the Congo basin show elevated flux values around 700 hPa (Figs. 5J and 5M). It is to be noted that the wind speed within AARs peaks around 650 hPa – suggesting the influence from the AEJ-South (AEJ-S ; Adebiyi and Zuidema, 2016; Chakraborty et al., 2021b; Das et al., 2017) on the AARs' wind profile (Figs. 7K and 7N) that might be responsible for the peaks in the aerosol mixing ratio profiles around 750 hPa (Figs. 5L and 5O) instead of the exponential profiles as observed in other regions. AARs over eastern China (blue) also carry a large amount of near-surface aerosol particles that contribute to large BC and OC IAT values in this region. Wind speed appears to have less influence on the flux profiles since the Indian Ocean and the Southern Ocean has the largest (smallest) wind speed (flux values) associated with the AARs.

4.4 Fraction of total annual transport accounted for by AARs

It is apparent from Figure 5 that the mean IAT averaged over AAR time steps is greater than the mean IAT averaged from all time steps. This is not surprising since AARs detected by our algorithm represent the extreme transport events (see Section 2 for definition and methodology). Considering that the original analysis on water vapor ARs (Zhu and Newell, 1998) highlighted that 90% of the poleward transport of water vapor in the midlatitudes occurred in a relativley small number of extreme transport events (i.e. ARs), a similar question can be raised here for AARs. Specifically, what fraction of the total annual aerosol transport is acounted for by the 20-40 AAR days that occur each year on average (Fig. 4)? Also, do AARs transport a higher fraction of the total global annual transport over the major aerosol transport pathways, and is this dependent on aerosol species? In Figure 6, we show the fraction of total annual IAT accouned for by AARs (shades), counting only the compoment of AAR transport in the direction of the

https://doi.org/10.5194/acp-2021-941
Preprint. Discussion started: 5 January 2022

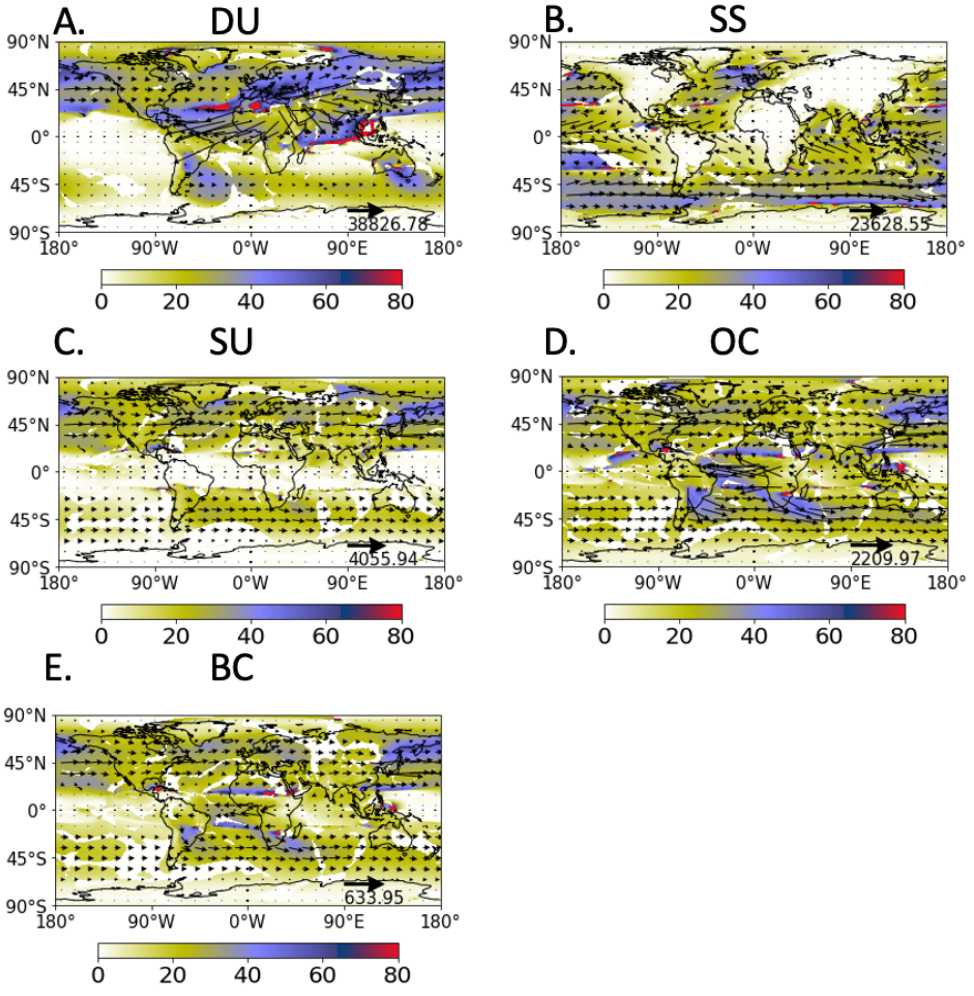

Figure 6. Fraction of annual total IAT transport (arrows; kg m^{-1}) accounted for by AARs (%; shading) of five different aerosol species.

380 total annual transport (arrows). Figure 6A shows that annually, ~ 40000-100000 kg m^{-1} of DU
381 IAT is transported by All events (i.e. considering all data points in the record) that originate from
382 the Sahara Desert. Near the equator, the fractional transport by AARs (F_{AAR}) is around ~20%
383 over the Atlantic Ocean in the direction of the Amazon rainforest (Fig. 6A), which is realized
384 within ~30 AAR days per year (see Fig. 4A). In this same longitude sector, F_{AAR} gradually

https://doi.org/10.5194/acp-2021-941
Preprint. Discussion started: 5 January 2022


Atmospheric Chemistry and Physics Discussions

385 increases with latitude and reaches over 80% around 35°-40° N where AARs act to transport dust
386 from the Sahara Desert to Europe and the middle-east region. Over Mongolia and China, the
387 total annual IAT is ~20000-40000 kg m^{-1} and about 30-40 AAR days per year (Fig .4A)
388 contribute to ~40-50% of that transport. In the Southern Hemisphere, Patagonia and South
389 American drylands give rise to ~4000 kg m^{-1} of annual dust transport and AARs contribute to 20-
390 40% of that transport in about 20-30 AAR events per year (Fig. 4A).

391 SS AARs are far more frequent over the oceans than over the land, (Figure 4B) with peak
392 frequencies of about 30 AAR days per year occurring over the subtropical trade wind regions,
393 Southern Ocean and northern Atlantic Ocean. In these regions, the total annual IAT is about
394 10000-20000 kg m^{-1}, and F_{AAR} is about ~ 20-30% in the subtropical regions, reaching ~50% over
395 the Southern Ocean and the North Atlantic Ocean (Fig. 6B).

396 AARs for other species of aerosols transport up to ~40% of the total annual IAT over their
397 major transport pathways. For example, the ~30 SU AAR days per year that originate over China
398 (Fig. 4C) transport ~30-40% of the total annual aerosol transport (~2500 kg m^{-1}) over the
399 northern Pacific Ocean. F_{AAR} associated with OC (BC) AARs is ~40% (30%) between the Congo
400 basin and the tropical Atlantic Ocean, China and the North Pacific Ocean, South Africa and the
401 Southern/Indian Oceans, south China and the west Pacific Ocean, and Amazon and the South
402 Atlantic Ocean/Southern Ocean. Higher F_{AAR} is also observed, despite low total annual IAT, over
403 the northern part of the Sahel region for both BC and OC AARs.

404 **4.5. AAR seasonality**

405 Figure 7 shows AAR frequency along with the direction and magnitude of the mean AAR
406 IAT during four different seasons. DU AARs (shading) originate during all the seasons over the
407 Sahara Desert. DU AAR IAT (arrows) is higher during DJF and MAM over the Sahara Desert

https://doi.org/10.5194/acp-2021-941
Preprint. Discussion started: 5 January 2022

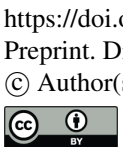

Atmospheric Chemistry and Physics Discussions

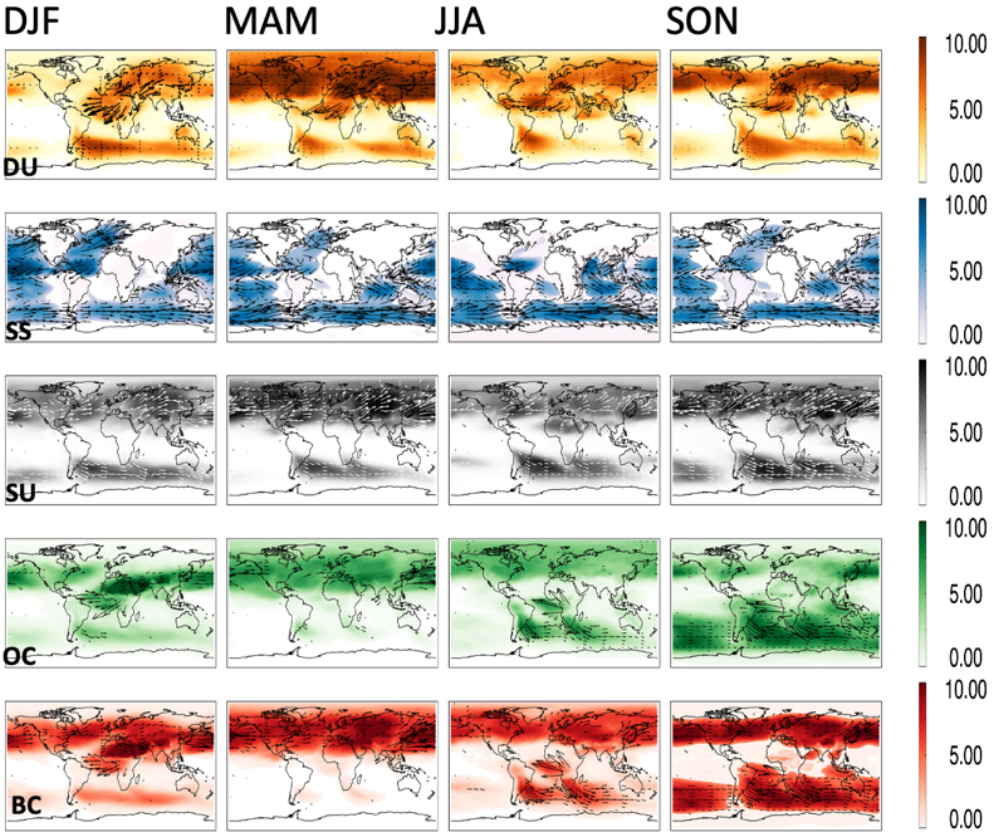

Figure 7. Seasonal variations of AAR frequency (days/season) and IAT (arrows) for five different species of aerosols.

408 owing to a stronger anticyclonic motion in the boreal winter and spring. The largest number of
409 DU AARs are generated during the MAM season when the DU IAT is the highest (Figure 1) and
410 widely spread across the Northern Hemisphere. In JJA and SON, DU AARs appear to have
411 lower IAT (shorter arrows), but are more frequent than in the DJF season. The frequency of SS
412 AARs also depends on the season. A higher number of SS AARs are detected over the eastern
413 Pacific Ocean and the west coast of the US, north Atlantic Ocean, and Europe in DJF and MAM.
414 In JJA, no SS AARs are detected over there. Over the Southern Ocean, SS AARs with large IAT

https://doi.org/10.5194/acp-2021-941
Preprint. Discussion started: 5 January 2022


Atmospheric Chemistry and Physics Discussions

415 are more frequent during austral winter or MAM and JJA. In comparison, tropical SS AARs are
416 present year-round.

417 SU AARs in the Northern Hemisphere are more (less) frequent in MAM (JJA) and can be
418 related to the seasonal variations in IAT there (Figure 1). The frequency of occurrences of SU
419 AARs is higher during SON compared to DJF while their IAT values are larger in DJF. This
420 might be because of the readiness of sulfate aerosols to form CCNs and their hygroscopic nature.
421 The occurrences of intense AR-related precipitation in DJF over the extratropical region in the
422 Northern Hemisphere might cause scavenging and wet removal of SU aerosols when the AARs
423 and ARs coexist. A detailed investigation considering AR-AAR interactions is needed in future
424 studies to better understand the coexistence and influence of AARs and ARs.

425 Over the Congo rainforest, several OC AARs occur during its dry season (also when CA
426 IAT is high, Fig. 1). A similar frequency of occurrences of OC AARs is also observed during the
427 dry season over the Amazon rainforest. Many OC AARs occur east of China during the DJF and
428 MAM season when the IAT values are large over there (Fig. 1). Many BC and OC AARs are
429 generated over the global rainforests during their dry seasons.

430 **4.6 Basic characteristics of individual AARs and algorithm sensitivities**

431 In this section, we characterize basic features of AARs (Fig. 8), including those related to
432 geometry and IAT intensity and directions, and discuss and show the sensitivity of various AAR
433 features to algorithm specifications and thresholds (Fig. 9). Fig. 8A shows that the frequency of
434 AARs decreases monotonically as AAR length increases for all aerosol species. The mean
435 lengths of DU, SS, SU, OC, BC AARs are 4264 km, 3722 km, 4121 km, 4528 km, and 4378 km,
436 respectively. Fig. 8B shows that AAR widths exhibit a skewed distribution, unlike AAR lengths,
437 implying an optimum or common value for AAR widths around 400 km. The mean width of DU,

https://doi.org/10.5194/acp-2021-941
Preprint. Discussion started: 5 January 2022

Atmospheric Chemistry and Physics Discussions

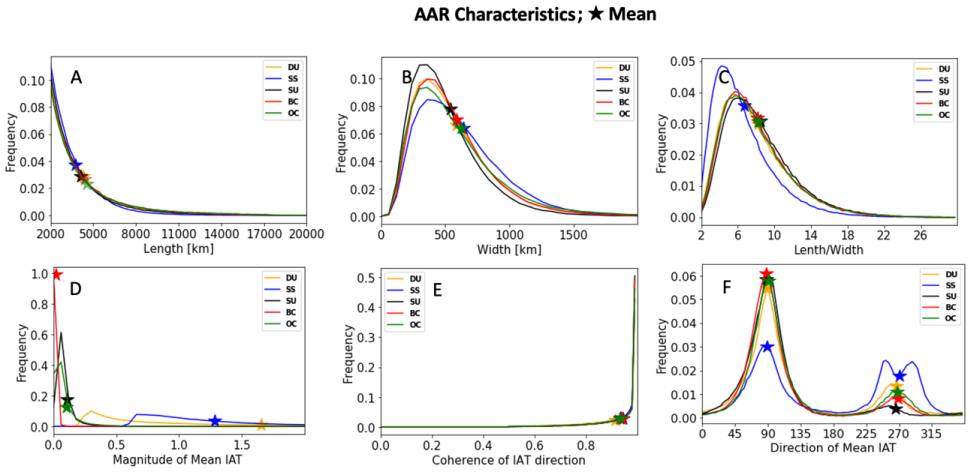

Figure 8. Histograms of characteristics of individual AARs. The "★" symbol denotes the mean. (A) Length. (B) Width. (C) Aspect ratio. (D) Magnitude of mean IAT. (E) Coherence of the IAT direction. (F) Direction of mean IAT.

SS, SU, OC, BC AARs is 586 km, 642 km, 542 km, 625 km, and 589 km, respectively. When considered together in the form of the aspect ratio of AARs, i.e., length/width ratio, the distribution is also a skewed distribution (Fig. 8C), with the lengths typically 6-8 times their widths. DU and SS AARs are the two species having the largest object-mean IAT values (Fig. 8D). While on average, DU AARs have IAT ~ 1.65 and 1.3 x 10^{-3} kg m^{-1} s^{-1}, respectively, SU, OC, and BC AARs have smaller IAT (Fig. 8D). Average object-mean IAT for SU, OC, and BC AARs are 0.1, 0.1, and 0.016 x 10^{-3} kg m^{-1} s^{-1}, respectively. The frequency of object-mean IAT for BC AARs decreases sharply and seldom reaches beyond 0.1 x 10^{-3} kg m^{-1} s^{-1}. SU (OC) AARs attain a maximum object-mean IAT values around 0.1 x 10^{-3} kg m^{-1} s^{-1} with a maximum frequency of ~0.6 (0.4).

The coherence of IAT directions (Fig. 8E) is computed as a fraction of the number of grid cells with IAT directed within 45° of the direction of the object-mean IAT to all the grid cells within that AAR. A large value implies that a larger fraction of the grid cells has IAT directed in

https://doi.org/10.5194/acp-2021-941
Preprint. Discussion started: 5 January 2022


Atmospheric Chemistry and Physics Discussions

451 the same overall direction as the AAR. AARs of all the species have the mean coherence of IAT
452 directions between 0.91 (DU) and 0.94 (SU). The distribution of the direction of the object-mean
453 IAT implies that the AARs are mostly directed in the zonal direction (Fig. 8F). Relative to North,
454 peak frequencies near 90° and between 250°- 310° imply that the AARs are either westerly or
455 easterly in nature. A few westerly AARs also transport aerosols in the northeastward (45°-90°)
456 and southeastward (90°-135°) directions. A wider peak between 250°- 310° implies that most of
457 the easterly AARs also have meridional components in the southwestward and northwestward
458 directions. The average values of object-mean IAT direction for all the species of AARs are ~90°
459 (westerly) and between 260-270° (easterly). These results show that the AARs mostly transport
460 aerosols in the zonal direction as compared to ARs that have notable transport of water vapor in
461 the meridional direction (Guan and Waliser, 2015).
462 Finally, Figure 9 shows the sensitivity of AAR detection in our algorithm to three primary
463 thresholds that define the geometry (length and aspect ratio) and grid-wise IAT limits (to identify
464 the extreme transport) of AARs. The results presented above in this study are based on a length
465 limit of 2000 km, aspect ratio limit of 2, and a pixel-wise IAT limit of the 85th percentile.
466 Keeping the length and aspect ratio limits fixed, while increasing the IAT limit to the 90th and
467 95th percentile values, yields fewer number of AARs detected (top row). On the other hand,
468 relaxing the length limit to 1750 km and 1500 km greatly increases the number of AARs
469 detected (middle row). Relaxing the aspect ratio limit to 1.5 and 1 does not significantly alter the
470 number of AARs detected, suggesting that the other limits applied (such as length greater than
471 2000 km) already effectively removes IAT objects that are not elongated. It appears from Figure
472 9 that grid-wise IAT thresholds pose a large sensitivity to AARs detection as the number of

https://doi.org/10.5194/acp-2021-941
Preprint. Discussion started: 5 January 2022

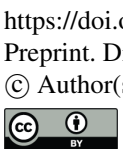

Atmospheric Chemistry and Physics Discussions

473 AARs detected is reduced roughly by half as we increase that threshold to the 95th percentile
474 from the 85th percentile used in our main analysis.

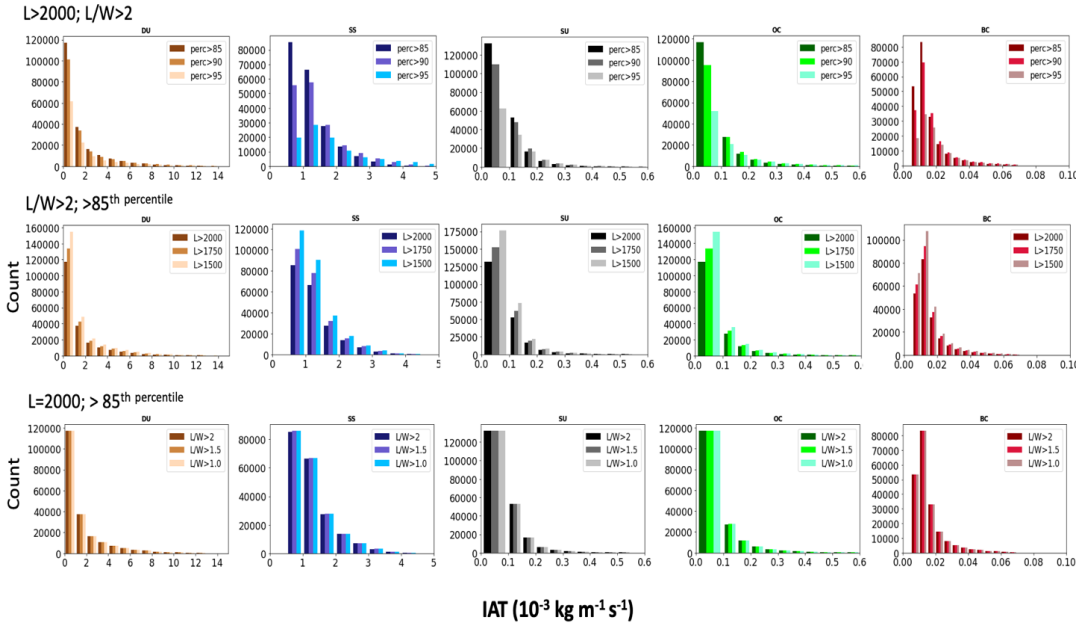

475

Figure 9. Sensitivity of AAR detection to threshold values used for three key parameters (corresponding to the three rows; see legend for the parameter being tested and the three values chosen for each test parameter) in the detection algorithm for five aerosol species (corresponding to the five columns; see panel title for the aerosol species). Shown are histograms of mean IAT of individual AARs detected. For example, the top row shows results based on perturbing the IAT percentile threshold (85th, 90th, and 95th percentiles) while keeping the length (2000 km) and aspect ratio (2) thresholds unchanged from the main analysis presented earlier.

476 Figure 10 shows the sensitivity of the global area coverage of AARs to AAR algorithm
477 parameters. Each bar represents the area-weighted global mean AAR frequency or a spatial-
478 temporal measure of the amount of time/space that there is an AAR. Annually, DU, SS, SU, OC,
479 and BC AARs cover 3.36% ,3.34% ,3.43% ,3.31% ,3.66% of the global area, respectively. Upon
480 relaxing the length limits to 1750 (1500) km increases the number of detections of AARs, thus

https://doi.org/10.5194/acp-2021-941
Preprint. Discussion started: 5 January 2022

Atmospheric Chemistry and Physics Discussions

481 the areal coverage of AARs increases to 3.45%-3.82% (3.59-3.97%). On the other hand,
482 increasing the pixel-wise IAT limit to 90th and 95th percentile reduces the areal coverage to
483 2.24%-2.62% and 0.87%-1.33%, respectively. Relaxing the aspect ratio doesn't have any impact
484 on AAR's areal coverage. ARs account for ~2% more of the Earth's surface area than AARs (not
485 shown), likely because the filter based on object-mean IVT direction in the AR algorithm
486 preferentially filtered out smaller objects compared to the revised filter in the AAR algorithm
487 based on IAT magnitude.

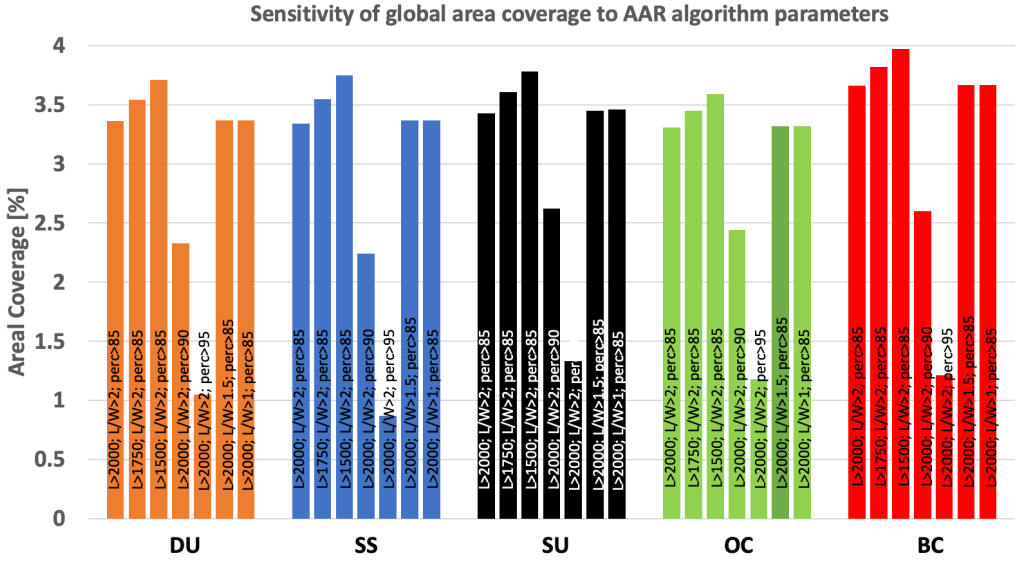

488

Figure 10. Sensitivity of AARs' and ARs' global area coverage to threshold values used for three key parameters in the detection algorithm. For each species of AARs, the first bar shows the global area coverage for the length limit >2000, aspect ratio > 2, and the pixel-wise IAT threshold >85%. Next two bars show the areal coverage after relaxing the length limit to 1750 and 1500 km. The fourth and the fifth bar shows the areal coverage after increasing the pixel-wise IAT limit to 90th and 95th percentile. The last two bars show the areal coverage after relaxing the aspect ratio to 1.5 and 1.

489 **5. Conclusions**

490 Using a newly developed AAR algorithm (Chakraborty et al, 2021a) based on the widely
491 used AR detection algorithm (Guan and Waliser, 2015), we examine a number of important

https://doi.org/10.5194/acp-2021-941
Preprint. Discussion started: 5 January 2022


Atmospheric Chemistry and Physics Discussions

492 details about AARs that were not explored in Chakraborty et al. (2021a). This includes AAR
493 seasonal variations in frequency and transport values (Fig. 7), the fraction of total annual aerosol
494 transport account for by AARs (Fig. 6), a characterization of their vertical profiles (Fig. 5),
495 relation to the pattern of surface emissions (Fig. 2), along with a number of basic characteristics
496 and distributions for quantities such as AAR length, aspect ratio, object-mean IAT, the coherence
497 of the direction of IAT (Fig. 8), and sensitivities of the algorithm to the thresholds chosen for
498 three key parameters (Fig.9).

499 Our results show that on average, 30-40 AAR days are responsible for more than 40% of
500 total annual aerosol transport for a given aerosol species over certain major transport pathways
501 around the globe. Over some regions of the world, DU and SS AARs can transport 60-100% of
502 the total annual aerosol transport of the respective species. The inhomogeneous nature of AARs'
503 spatial distribution and fractional transport out of the annual total suggest a plausible impact of
504 the AARs on the meridional temperature gradient. The attenuation of solar energy by AARs
505 might impact the surface temperature, thus can alter the meridional temperature gradient and the
506 thermal winds. Further analysis will be conducted in the future to delineate the impacts of AARs
507 on the global weather and climate.

508 The major transport pathways by AARs are also identified in our algorithm for each of the
509 aerosol species. The source of AARs is consistent with the major aerosol emission regions of the
510 world. DU aerosols are mostly originated from the global deserts and their frequency is higher
511 during boreal autumn and spring. SS AARs are mostly located over the global oceans and carry
512 the footprint of the storms. In the midlatitudes their frequency and intensity increase during the
513 boreal (austral) winter in the Northern (Southern) Hemisphere. Tropical SS AARs are more
514 frequent, but their magnitude of aerosol transport and contribution to the annual aerosol transport

https://doi.org/10.5194/acp-2021-941
Preprint. Discussion started: 5 January 2022


Atmospheric Chemistry and Physics Discussions

515 is less. A further investigation is needed to understand if/how tropical cyclones and midlatitude
516 storms impact SS AARs differently. CA AARs are generated over the region where biomass
517 burning is more common like India and China. CA AARs that originate from the global
518 rainforests have the highest frequency as well as intensity during their dry seasons, but are
519 mostly absent or exist with a reduced frequency during their wet seasons. SU AARs are present
520 year around in the northern hemisphere owing to the biomass burning and biogenic activities
521 over there with a peak frequency and intensity during the boreal spring and autumn. Overall,
522 regions with frequent AAR activities include the Sahara Desert-Caribbean and Europe for DU
523 AARs, a circumpolar transport around the midlatitude region in the northern hemisphere for all
524 but SS AARs, global oceans and midlatitude storm tracks over the global ocean for SS AARs,
525 global rainforests for BC and OC AARs, and from South America and Africa to the Southern
526 Ocean for DU, BC, OC, and SU AARs.

527 We have also examined the vertical structure of aerosol mixing ratio and wind inside AARs.
528 Over most of the major pathways, aerosol mixing ratio and flux values decrease with height. A
529 higher aerosol mass mixing ratio inside AARs is observed below the 700 hPa over most of the
530 regions and thus, may have a strong implication on the low cloud cover and surface irradiance.
531 Such an interaction can be complex since shallow clouds also have cooling effects as most of the
532 aerosol species do. Understanding such an interaction between shallow clouds and AARs and
533 their impacts on the cooling effect warrants further investigation. The aerosol mixing ratio (wind
534 speed) appears to contribute a large fraction of IAT below (above) 700 hPa. However, AARs
535 generated from the African continent are the exceptions. Signatures of AEJ-N on DU AARs
536 taking off the Sahara Desert and AEJ-S on BC/OC AARs originated from the Congo basin are
537 observed. Both the aerosol mixing ratio and wind speed appear to peak around 600-700 hPa,

https://doi.org/10.5194/acp-2021-941
Preprint. Discussion started: 5 January 2022


Atmospheric Chemistry and Physics Discussions

538 leading to a higher IAT at the level. The fact that aerosols are lifted up and attain a peak mass
539 flux around the 700 hPa for AARs generated from the African continent might have a strong
540 influence on the wet season onset and rainfall mechanisms over there (Chakraborty et al.,
541 2021b). In a future study, an in-depth analysis will be performed using the observation from the
542 ORACLES mission and Cloud-Aerosol Lidar and Infrared Pathfinder Satellite Observation to
543 study the subsidence that depresses the plumes once they reach the Atlantic Ocean off the west
544 African Coast (Das et al., 2017).

545 AAR frequency of occurrence decreases monotonically with its length with the mean length
546 around 4000 km. However, AAR width and aspect ratio show a skewed distribution. AAR length
547 is, on average, 6-8 times the width. DU and SS AARs carry a larger amount of aerosol mass as
548 compared to SU, OC, and BC aerosols. More than 90% of all the grid cells within an individual
549 AAR have IAT directed in the same overall direction of the AAR, showing that the transport
550 occurring inside an individual AAR is largely coherent in direction. AARs are mostly oriented in
551 the zonal direction. A peak frequency of the direction of object-mean IAT is observed between
552 45°-135° (westerly AARs) or 225°-315° (easterly AARs). Large mean width and length (Figure
553 8A and 8B) of AARs imply that AARs have a significant amount of areal cover. AARs also
554 transport a higher aerosol mass mixing ratio, located mostly in the lower troposphere, to regions
555 far from their sources – often intercontinental 20-40 days per year on average. Our findings, thus,
556 indicate the necessity of exploring the impacts of AARs on human health since smoke as well as
557 dust particles and the secondary aerosol particles that can be generated over the AAR lifetime
558 might have a huge impact on human health, especially on lungs. The algorithm shows little to no
559 sensitivity to the aspect ratio limit chosen, but notable influence of the length limit, and strongest
560 influence of the IAT percentile limit on the detection result.

https://doi.org/10.5194/acp-2021-941
Preprint. Discussion started: 5 January 2022


Atmospheric Chemistry and Physics Discussions

561 This study points out the necessity to analyze and investigate the impact of AARs on climate
562 and air quality. The fact that AARs can carry a greater number of aerosol particles through a
563 narrow pathway and probably can contain more aerosol particles than a moderate-high AOD
564 region suggests that their impact on radiative forcing and cloud microphysics can be stronger
565 than that have been reported and investigated so far in the literature. We have not addressed the
566 role of climate modulation on AAR activity and characteristics. Events like El Niño, La Niña,
567 Pacific Decadal Oscillation, North American Subtropical High, Madden-Julian Oscillations can
568 have a significant influence on AARs and will be addressed in future studies. A further
569 investigation is needed on the AR and AAR interaction and how ARs and cyclonic activities
570 modulate AARs in the midlatitude during the winter season of each hemisphere.

571 **Author Contribution:**

572 SC, BG, DW, and AMS designed the research and wrote the paper. SC analyzed the data.

573 **Competing Interests:**

574 The authors have no competing interests.

575 **Data and Code Availability**

576 All satellite data used in this study can be downloaded at the EOSDIS Distributed Active
577 Archive Centers (DAACs) at https://earthdata.nasa.gov/eosdis/daacs. References about the
578 datasets have been provided in the Data section (Sect. 2). Please contact the corresponding author
579 for any questions about how to download the data that are publicly available and codes written in
580 IDL and Python. The AAR data set will be made publicly available after the publication. The AAR
581 code is available from B.G. on request.

582 **Acknowledgements:**

583 This work was supported by the National Aeronautics and Space Administration. The

https://doi.org/10.5194/acp-2021-941
Preprint. Discussion started: 5 January 2022


Atmospheric Chemistry and Physics Discussions

584 contribution of S.C. and D.W. was carried out on behalf of the Jet Propulsion Laboratory,
585 California Institute of Technology, under a contract with NASA. All the data are publicly
586 available and free to download. Please see reference section for the citations to all the data sets
587 used in this study. Also, details about the dataset have been included in the supplementary
588 section.

589 **References**

590
591 Adebiyi, A. A. and Zuidema, P.: The role of the southern African easterly jet in modifying the
592 southeast Atlantic aerosol and cloud environments, Q. J. R. Meteorol. Soc., doi:10.1002/qj.2765,
593 2016.
594 Aldabash, M., Balcik, F. B. and Glantz, P.: Validation of MODIS C6.1 and MERRA-2 AOD
595 using AERONET observations: A comparative study over Turkey, Atmosphere (Basel).,
596 doi:10.3390/ATMOS11090905, 2020.
597 Andreae, M. O. and Rosenfeld, D.: Aerosol-cloud-precipitation interactions. Part 1. The nature
598 and sources of cloud-active aerosols, Earth-Science Rev., doi:10.1016/j.earscirev.2008.03.001,
599 2008.
600 Bister, M. and Kulmala, M.: Anthropogenic aerosols may have increased upper tropospheric
601 humidity in the 20th century, Atmos. Chem. Phys., doi:10.5194/acp-11-4577-2011, 2011.
602 Buchard, V., Randles, C. A., da Silva, A. M., Darmenov, A., Colarco, P. R., Govindaraju, R.,
603 Ferrare, R., Hair, J., Beyersdorf, A. J., Ziemba, L. D. and Yu, H.: The MERRA-2 aerosol
604 reanalysis, 1980 onward. Part II: Evaluation and case studies, J. Clim., doi:10.1175/JCLI-D-16-
605 0613.1, 2017.
606 Carra, E., Marzo, A., Ballestrín, J., Polo, J., Barbero, J., Alonso-Montesinos, J., Monterreal, R.,
607 Abreu, E. F. M. and Fernández-Reche, J.: Atmospheric extinction levels of solar radiation using

608 aerosol optical thickness satellite data. Validation methodology with measurement system,
609 Renew. Energy, doi:10.1016/j.renene.2019.10.106, 2020.
610 Chakraborty, S., Fu, R., Massie, S. T. and Stephens, G.: Relative influence of meteorological
611 conditions and aerosols on the lifetime of mesoscale convective systems, Proc. Natl. Acad. Sci.
612 U. S. A., doi:10.1073/pnas.1601935113, 2016.
613 Chakraborty, S., Fu, R., Rosenfeld, D. and Massie, S. T.: The Influence of Aerosols and
614 Meteorological Conditions on the Total Rain Volume of the Mesoscale Convective Systems
615 Over Tropical Continents, Geophys. Res. Lett., 45(23), 13,13-99,106,
616 doi:10.1029/2018GL080371, 2018.
617 Chakraborty, S., Guan, B., Waliser, D. E., da Silva, A. M., Uluatam, S. and Hess, P.: Extending
618 the Atmospheric River Concept to Aerosols: Climate and Air Quality Impacts, Geophys. Res.
619 Lett., doi:10.1029/2020GL091827, 2021a.
620 Chakraborty, S., Jiang, J. H., Su, H. and Fu, R.: On the Role of Aerosol Radiative Effect in the
621 Wet Season Onset Timing over the Congo Rainforest during Boreal Autumn, Atmos. Chem.
622 Phys. Discuss., 2021, 1–27, doi:10.5194/acp-2020-1138, 2021b.
623 Chapman, W. E., Subramanian, A. C., Delle Monache, L., Xie, S. P. and Ralph, F. M.:
624 Improving Atmospheric River Forecasts With Machine Learning, Geophys. Res. Lett.,
625 doi:10.1029/2019GL083662, 2019.
626 Chylek, P. and Wong, J.: Effect of absorbing aerosols on global radiation budget, Geophys. Res.
627 Lett., doi:10.1029/95GL00800, 1995.
628 Cook, K. H.: Generation of the African easterly jet and its role in determining West African
629 precipitation, J. Clim., doi:10.1175/1520-0442(1999)012<1165:GOTAEJ>2.0.CO;2, 1999.
630 Dai, Q., Bi, X., Song, W., Li, T., Liu, B., Ding, J., Xu, J., Song, C., Yang, N., Schulze, B. C.,

https://doi.org/10.5194/acp-2021-941
Preprint. Discussion started: 5 January 2022


Atmospheric Chemistry and Physics Discussions

631 Zhang, Y., Feng, Y. and Hopke, P. K.: Residential coal combustion as a source of primary
632 sulfate in Xi'an, China, Atmos. Environ., doi:10.1016/j.atmosenv.2018.10.002, 2019.
633 Das, S., Harshvardhan, H., Bian, H., Chin, M., Curci, G., Protonotariou, A. P., Mielonen, T.,
634 Zhang, K., Wang, H. and Liu, X.: Biomass burning aerosol transport and vertical distribution
635 over the South African-Atlantic region, J. Geophys. Res., doi:10.1002/2016JD026421, 2017.
636 Dhana Laskhmi, D. and Satyanarayana, A. N. V.: Climatology of landfalling atmospheric Rivers
637 and associated heavy precipitation over the Indian coastal regions, Int. J. Climatol.,
638 doi:10.1002/joc.6540, 2020.
639 Edwards, T. K., Smith, L. M. and Stechmann, S. N.: Atmospheric rivers and water fluxes in
640 precipitating quasi-geostrophic turbulence, Q. J. R. Meteorol. Soc., doi:10.1002/qj.3777, 2020.
641 Fan, J., Wang, Y., Rosenfeld, D. and Liu, X.: Review of aerosol-cloud interactions: Mechanisms,
642 significance, and challenges, J. Atmos. Sci., doi:10.1175/JAS-D-16-0037.1, 2016.
643 Froyd, K. D., Murphy, D. M., Sanford, T. J., Thomson, D. S., Wilson, J. C., Pfister, L. and Lait,
644 L.: Aerosol composition of the tropical upper troposphere, Atmos. Chem. Phys.,
645 doi:10.5194/acp-9-4363-2009, 2009.
646 Gelaro, R., McCarty, W., Suárez, M. J., Todling, R., Molod, A., Takacs, L., Randles, C. A.,
647 Darmenov, A., Bosilovich, M. G., Reichle, R., Wargan, K., Coy, L., Cullather, R., Draper, C.,
648 Akella, S., Buchard, V., Conaty, A., da Silva, A. M., Gu, W., Kim, G.-K., Koster, R., Lucchesi,
649 R., Merkova, D., Nielsen, J. E., Partyka, G., Pawson, S., Putman, W., Rienecker, M., Schubert,
650 S. D., Sienkiewicz, M. and Zhao, B.: The Modern-Era Retrospective Analysis for Research and
651 Applications, Version 2 (MERRA-2), J. Clim., 30(14), 5419–5454, doi:10.1175/JCLI-D-16-
652 0758.1, 2017.
653 Gibson, P. B., Waliser, D. E., Guan, B., Deflorio, M. J., Ralph, F. M. and Swain, D. L.: Ridging

https://doi.org/10.5194/acp-2021-941
Preprint. Discussion started: 5 January 2022


Atmospheric Chemistry and Physics Discussions

654 associated with Drought across the Western and Southwestern United States: Characteristics,
655 trends, and predictability sources, J. Clim., doi:10.1175/JCLI-D-19-0439.1, 2020.
656 Global Modeling and Assimilation Office (GMAO): MERRA-2 tavg1_2d_aer_Nx: 2d,1-
657 Hourly,Time-averaged,Single-Level,Assimilation,Aerosol Diagnostics V5.12.4, Greenbelt, MD,
658 USA., 2015a.
659 Global Modeling and Assimilation Office (GMAO): MERRA-2 tavgU_2d_adg_Nx:
660 2d,diurnal,Time-averaged,Single-Level,Assimilation,Aerosol Diagnostics (extended) V5.12.4,
661 Greenbelt, MD, USA., 2015b.
662 Gross, A. and Baklanov, A.: Aerosol Production in the Marine Boundary Layer Due to
663 Emissions from DMS: Study Based on Theoretical Scenarios Guided by Field Campaign Data, in
664 Air Pollution Modeling and Its Application XVII., 2007.
665 Guan, B. and Waliser, D. E.: Detection of atmospheric rivers: Evaluation and application of an
666 algorithm for global studies, J. Geophys. Res., doi:10.1002/2015JD024257, 2015.
667 Guan, B. and Waliser, D. E.: Tracking Atmospheric Rivers Globally: Spatial Distributions and
668 Temporal Evolution of Life Cycle Characteristics, J. Geophys. Res. Atmos.,
669 doi:10.1029/2019JD031205, 2019.
670 Guan, B., Waliser, D. E. and Martin Ralph, F.: An intercomparison between reanalysis and
671 dropsonde observations of the total water vapor transport in individual atmospheric rivers, J.
672 Hydrometeorol., doi:10.1175/JHM-D-17-0114.1, 2018.
673 Guan, B., Waliser, D. E. and Ralph, F. M.: A multimodel evaluation of the water vapor budget in
674 atmospheric rivers, Ann. N. Y. Acad. Sci., doi:10.1111/nyas.14368, 2020.
675 Gueymard, C. A. and Yang, D.: Worldwide validation of CAMS and MERRA-2 reanalysis
676 aerosol optical depth products using 15 years of AERONET observations, Atmos. Environ.,

677 doi:10.1016/j.atmosenv.2019.117216, 2020.
678 Gupta, P. and Christopher, S. A.: Particulate matter air quality assessment using integrated
679 surface, satellite, and meteorological products: 2. A neural network approach, J. Geophys. Res.
680 Atmos., doi:10.1029/2008JD011497, 2009.
681 Huang, Y., Dickinson, R. E. and Chameides, W. L.: Impact of aerosol indirect effect on surface
682 temperature over East Asia, Proc. Natl. Acad. Sci. U. S. A., doi:10.1073/pnas.0504428103, 2006.
683 Huning, L. S., Guan, B., Waliser, D. E. and Lettenmaier, D. P.: Sensitivity of Seasonal Snowfall
684 Attribution to Atmospheric Rivers and Their Reanalysis-Based Detection, Geophys. Res. Lett.,
685 doi:10.1029/2018GL080783, 2019.
686 IPCC: Climate Change 2013: The Physical Science Basis. Contribution of Working Group I to
687 the Fifth Assessment Report of the Intergovernmental Panel on Climate Change., 2013a.
688 IPCC: Working Group I Contribution to the IPCC Fifth Assessment Report, Climate Change
689 2013: The Physical Science Basis, Ipcc, AR5(March 2013), 2014,
690 doi:10.1017/CBO9781107415324.Summary, 2013b.
691 Jennrich, G. C., Furtado, J. C., Basara, J. B. and Martin, E. R.: Synoptic Characteristics of 14-
692 Day Extreme Precipitation Events across the United States, J. Clim., doi:10.1175/JCLI-D-19-
693 0563.1, 2020.
694 Keil, A. and Haywood, J. M.: Solar radiative forcing by biomass burning aerosol particles during
695 SAFARI 2000: A case study based on measured aerosol and cloud properties, J. Geophys. Res.
696 Atmos., doi:10.1029/2002jd002315, 2003.
697 Khain, A. P., BenMoshe, N. and Pokrovsky, A.: Factors determining the impact of aerosols on
698 surface precipitation from clouds: An attempt at classification, J. Atmos. Sci.,
699 doi:10.1175/2007JAS2515.1, 2008.

https://doi.org/10.5194/acp-2021-941
Preprint. Discussion started: 5 January 2022


Atmospheric Chemistry and Physics Discussions

700 Kim, D. and Ramanathan, V.: Solar radiation budget and radiative forcing due to aerosols and
701 clouds, J. Geophys. Res. Atmos., doi:10.1029/2007JD008434, 2008.
702 Li, Z., Guo, J., Ding, A., Liao, H., Liu, J., Sun, Y., Wang, T., Xue, H., Zhang, H. and Zhu, B.:
703 Aerosol and boundary-layer interactions and impact on air quality, Natl. Sci. Rev.,
704 doi:10.1093/nsr/nwx117, 2017.
705 Lohmann, U. and Feichter, J.: Can the direct and semi-direct aerosol effect compete with the
706 indirect effect on a global scale?, Geophys. Res. Lett., doi:10.1029/2000GL012051, 2001.
707 Martin, R. V.: Satellite remote sensing of surface air quality, Atmos. Environ.,
708 doi:10.1016/j.atmosenv.2008.07.018, 2008.
709 May, N. W., Quinn, P. K., McNamara, S. M. and Pratt, K. A.: Multiyear study of the dependence
710 of sea salt aerosol on wind speed and sea ice conditions in the coastal Arctic, J. Geophys. Res.,
711 doi:10.1002/2016JD025273, 2016.
712 McComiskey, A. and Feingold, G.: Quantifying error in the radiative forcing of the first aerosol
713 indirect effect, Geophys. Res. Lett., doi:10.1029/2007GL032667, 2008.
714 Mishra, A. K., Koren, I. and Rudich, Y.: Effect of aerosol vertical distribution on aerosol-
715 radiation interaction: A theoretical prospect, Heliyon, doi:10.1016/j.heliyon.2015.e00036, 2015.
716 Nash, D. and Carvalho, L.: Brief Communication: An Electrifying Atmospheric River:
717 Understanding the Thunderstorm Event in Santa Barbara County during March 2019, Nat.
718 Hazards Earth Syst. Sci., doi:10.5194/nhess-2019-342, 2019.
719 Ralph, F. M., Dettinger, M. D., Rutz, J. J. and Waliser, D. E.: Atmospheric Rivers, 2020th ed.,
720 n.d.
721 Randles, C. A., da Silva, A. M., Buchard, V., Colarco, P. R., Darmenov, A., Govindaraju, R.,
722 Smirnov, A., Holben, B., Ferrare, R., Hair, J., Shinozuka, Y. and Flynn, C. J.: The MERRA-2

https://doi.org/10.5194/acp-2021-941
Preprint. Discussion started: 5 January 2022


Atmospheric Chemistry and Physics Discussions

723 aerosol reanalysis, 1980 onward. Part I: System description and data assimilation evaluation, J.
724 Clim., doi:10.1175/JCLI-D-16-0609.1, 2017.
725 Rosenfeld, D., Lohmann, U., Raga, G. B., O'Dowd, C. D., Kulmala, M., Fuzzi, S.,
726 Reissell, A. and Andreae, M. O.: Flood or Drought: How Do Aerosols Affect Precipitation?,
727 Science (80-.)., 321(5894), 1309 LP – 1313, doi:10.1126/science.1160606, 2008.
728 Rosenfeld, D., Wood, R., Donner, L. J. and Sherwood, S. C.: Aerosol Cloud-Mediated Radiative
729 Forcing: Highly Uncertain and Opposite Effects from Shallow and Deep Clouds, in Climate
730 Science for Serving Society: Research, Modeling and Prediction Priorities, edited by G. R. Asrar
731 and J. W. Hurrell, pp. 105–149, Springer Netherlands, Dordrecht., 2013.
732 Rosenfeld, D., Andreae, M. O., Asmi, A., Chin, M., Leeuw, G., Donovan, D. P., Kahn, R.,
733 Kinne, S., Kivekäs, N., Kulmala, M., Lau, W., Schmidt, K. S., Suni, T., Wagner, T., Wild, M.
734 and Quaas, J.: Global observations of aerosol-cloud-precipitation- climate interactions, Rev.
735 Geophys, 52, 750–808, doi:10.1002/2013RG000441.Received, 2014.
736 Rosenfeld, D., Zheng, Y., Hashimshoni, E., Pöhlker, M. L., Jefferson, A., Pöhlker, C., Yu, X.,
737 Zhu, Y., Liu, G., Yue, Z., Fischman, B., Li, Z., Giguzin, D., Goren, T., Artaxo, P., Barbosa, H.
738 M. J., Pöschl, U. and Andreae, M. O.: Satellite retrieval of cloud condensation nuclei
739 concentrations by using clouds as CCN chambers, Proc. Natl. Acad. Sci. U. S. A.,
740 doi:10.1073/pnas.1514044113, 2016.
741 Satheesh, S. K. and Ramanathan, V.: Large differences in tropical aerosol forcing at the top of
742 the atmosphere and Earth's surface, Nature, doi:10.1038/35011039, 2000.
743 Seinfeld, J. H., Bretherton, C., Carslaw, K. S., Coe, H., DeMott, P. J., Dunlea, E. J., Feingold, G.,
744 Ghan, S., Guenther, A. B., Kahn, R., Kraucunas, I., Kreidenweis, S. M., Molina, M. J., Nenes,
745 A., Penner, J. E., Prather, K. A., Ramanathan, V., Ramaswamy, V., Rasch, P. J., Ravishankara,

https://doi.org/10.5194/acp-2021-941
Preprint. Discussion started: 5 January 2022


Atmospheric Chemistry and Physics Discussions

746 A. R., Rosenfeld, D., Stephens, G. and Wood, R.: Improving our fundamental understanding of
747 the role of aerosol–cloud interactions in the climate system, Proc. Natl. Acad. Sci., 113(21),
748 5781–5790, doi:10.1073/pnas.1514043113, 2016.
749 Sharma, A. R. and Déry, S. J.: Variability and trends of landfalling atmospheric rivers along the
750 Pacific Coast of northwestern North America, Int. J. Climatol., doi:10.1002/joc.6227, 2020.
751 Sitnov, S. A., Mokhov, I. I. and Likhosherstova, A. A.: Exploring large-scale black-carbon air
752 pollution over Northern Eurasia in summer 2016 using MERRA-2 reanalysis data, Atmos. Res.,
753 doi:10.1016/j.atmosres.2019.104763, 2020.
754 Sofiev, M., Soares, J., Prank, M., De Leeuw, G. and Kukkonen, J.: A regional-to-global model of
755 emission and transport of sea salt particles in the atmosphere, J. Geophys. Res. Atmos.,
756 doi:10.1029/2010JD014713, 2011.
757 Stevens, B. and Feingold, G.: Untangling aerosol effects on clouds and precipitation in a
758 buffered system, Nature, doi:10.1038/nature08281, 2009.
759 Takemura, T., Nozawa, T., Emori, S., Nakajima, T. Y. and Nakajima, T.: Simulation of climate
760 response to aerosol direct and indirect effects with aerosol transport-radiation model, J. Geophys.
761 Res. D Atmos., doi:10.1029/2004JD005029, 2005.
762 Wang, J. and Christopher, S. A.: Intercomparison between satellite-derived aerosol optical
763 thickness and PM2.5 mass: Implications for air quality studies, Geophys. Res. Lett.,
764 doi:10.1029/2003GL018174, 2003.
765 Wang, X., Wang, C., Wu, J., Miao, G., Chen, M., Chen, S., Wang, S., Guo, Z., Wang, Z., Wang,
766 B., Li, J., Zhao, Y., Wu, X., Zhao, C., Lin, W., Zhang, Y. and Liu, L.: Intermediate Aerosol
767 Loading Enhances Photosynthetic Activity of Croplands, Geophys. Res. Lett.,
768 doi:10.1029/2020GL091893, 2021.

https://doi.org/10.5194/acp-2021-941
Preprint. Discussion started: 5 January 2022


Atmospheric Chemistry and Physics Discussions

769 Wang, Y., Zhang, Q. Q., He, K., Zhang, Q. and Chai, L.: Sulfate-nitrate-ammonium aerosols
770 over China: Response to 2000-2015 emission changes of sulfur dioxide, nitrogen oxides, and
771 ammonia, Atmos. Chem. Phys., doi:10.5194/acp-13-2635-2013, 2013.
772 Wang, Z., Walsh, J., Szymborski, S. and Peng, M.: Rapid arctic sea ice loss on the synoptic time
773 scale and related atmospheric circulation anomalies, J. Clim., doi:10.1175/JCLI-D-19-0528.1,
774 2020.
775 Wu, M. L. C., Reale, O., Schubert, S. D., Suarez, M. J., Koster, R. D. and Pegion, P. J.: African
776 easterly jet: Structure and maintenance, J. Clim., doi:10.1175/2009JCLI2584.1, 2009.
777 Xi, X. and Sokolik, I. N.: Impact of Asian Dust Aerosol and Surface Albedo on
778 Photosynthetically Active Radiation and Surface Radiative Balance in Dryland Ecosystems,
779 edited by D. G. Kaskaoutis, Adv. Meteorol., 2012, 276207, doi:10.1155/2012/276207, 2012.
780 Xu, X., Wu, H., Yang, X. and Xie, L.: Distribution and transport characteristics of dust aerosol
781 over Tibetan Plateau and Taklimakan Desert in China using MERRA-2 and CALIPSO data,
782 Atmos. Environ., doi:10.1016/j.atmosenv.2020.117670, 2020.
783 Zhou, Y. and Kim, H.: Impact of Distinct Origin Locations on the Life Cycles of Landfalling
784 Atmospheric Rivers Over the U.S. West Coast, J. Geophys. Res. Atmos.,
785 doi:10.1029/2019JD031218, 2019.
786 Zhu, Y. and Newell, R. E.: Atmospheric rivers and bombs, Geophys. Res. Lett.,
787 doi:10.1029/94GL01710, 1994.
788 Zhu, Y. and Newell, R. E.: A proposed algorithm for moisture fluxes from atmospheric rivers,
789 Mon. Weather Rev., doi:10.1175/1520-0493(1998)126<0725:APAFMF>2.0.CO;2, 1998.
790